

# Dynamical Rotational Instability at Low $T/W$

Joan M. Centrella<sup>1</sup>, Kimberly C. B. New<sup>2,3</sup>, Lisa L. Lowe<sup>1</sup>, and J. David Brown<sup>4</sup>

## ABSTRACT

Dynamical instability is shown to occur in differentially rotating polytropes with  $N = 3.33$  and  $T/|W| \gtrsim 0.14$ . This instability has a strong  $m = 1$  mode, although the  $m = 2, 3$ , and 4 modes also appear. Such instability may allow a centrifugally-hung core to begin collapsing to neutron star densities on a dynamical timescale. The gravitational radiation emitted by such unstable cores may be detectable with advanced ground-based detectors, such as LIGO II. If the instability occurs in a supermassive star, it may produce gravitational radiation detectable by the space-based detector LISA.

*Subject headings:* instabilities — gravitation — hydrodynamics — stars: rotation — stars: neutron

## 1. Introduction

Rotational instabilities are potentially important in the evolution of massive stellar cores. For example, the core of a massive star that has been prevented from collapsing to neutron star densities by centrifugal forces may rotate rapidly enough for rotational instabilities to develop (Hayashi, Eriguchi, & Hashimoto 1998, 1999). Massive cores spun up by accretion from a binary companion (Wagoner 1984) and the remnants of compact binary mergers (Rasio & Shapiro 1992; Zhuge, Centrella, & McMillan 1994) may also reach fast enough rotation rates to become unstable. Rotational instabilities may produce detectable gravitational radiation (Schutz 1989; Thorne 1996). If enough angular momentum is shed, full collapse to a neutron star or black hole may occur.

We focus here on global rotational instabilities that arise in fluids from growing azimuthal modes  $e^{im\phi}$  (Tassoul 1978). Dynamical instabilities are driven by hydrodynamics and gravity, and grow on the order of the dynamical timescales of the

system. In objects with Maclaurin-like rotation laws, dynamical rotational instabilities are generally expected to arise at fairly high values of  $\beta \equiv T/|W| \gtrsim 0.27$  in Newtonian gravity (see New, Centrella, & Tohline and references therein), and  $\beta \gtrsim 0.25 - 0.26$  in general relativity (Shibata, Baumgarte, & Shapiro 2000). Here,  $T$  is the rotational kinetic energy, and  $W$  is the gravitational potential energy. Dynamical instability may set in at lower values of  $\beta$  for thick, self-gravitating disks (Pickett, Durisen, & Davis 1996; Woodward, Tohline, & Hachisu 1994) and in tori (Tohline & Hachisu 1990). Secular instabilities develop on longer timescales, and arise from dissipative processes such as viscosity and gravitational radiation reaction. They are expected to set in for relatively low values of  $\beta \gtrsim 0.14$ , although the rotation law, polytropic index, and general relativity can affect the value of the instability limit (Imamura, et al. 1995; Stergioulas & Friedman 1998).

Studies of scenarios for the formation of centrifugally-hung cores have generally concluded that these objects will have  $\beta < 0.27$  (Tohline 1984; Eriguchi & Müller 1985; Müller & Eriguchi 1985). Direct numerical simulations of axisymmetric stellar collapse by Zwerger & Müller (1997) also indicate that, for the cases studied, it is difficult for collapsing cores to reach and exceed  $\beta \sim 0.27$ . Overall, it is generally assumed that centrifugally-hung cores will evolve secularly, as in the “fizzler” scenario

<sup>1</sup>Department of Physics, Drexel University, Philadelphia, PA 19104

<sup>2</sup>X-2, MS B-220, Los Alamos National Laboratory, Los Alamos, NM 87545

<sup>3</sup>The initial stage of this work was conducted while New was at the Department of Physics, Drexel University.

<sup>4</sup>Department of Physics, North Carolina State University, Raleigh, NC 27695

(Hayashi, Eriguchi, & Hashimoto 1998, 1999).

In this *Letter*, we report on new 3-D numerical simulations of rotating stellar cores that exhibit dynamical rotational instability at relatively low values of  $\beta \gtrsim 0.14$ . These models are computed using Newtonian gravity with no backreaction; this is a reasonable approximation for a stellar core of mass  $M \sim 1.4M_\odot$  hung up at a radius  $R \gtrsim 100\text{km}$ , so that  $(GM/Rc^2) \lesssim 0.02$ . Our results show that compact objects can become dynamically unstable in a region of parameter space previously thought to be solely the province of secular instabilities.

## 2. Numerical Simulations

Rotating stellar cores are initially assumed to be axisymmetric equilibrium polytropes with equation of state  $P = K\rho^\Gamma = K\rho^{1+1/N}$ , with  $\Gamma = 1.3$  ( $N = 3.33$ ). The angular velocity distribution is given by the so-called  $j$ -constant rotation law,  $\Omega^2 = j_o^2/(d^2 + \varpi^2)^2$ , where  $\varpi$  is the cylindrical radius and  $d$  is an arbitrary constant (Hachisu 1986). As  $d \rightarrow 0$ , the specific angular momentum approaches the constant value  $j_o$ . Here, we use  $d = 0.2$ . The models are computed on a uniformly spaced  $(\varpi, z)$  grid using the self-consistent field method of Hachisu (1986). Varying the axis ratio yields equilibria with different values of  $\beta$ ; see New, Centrella, & Tohline (2000) for details. Figure 1 shows density contours in the  $x - z$  plane for the 4 models that we evolved here,  $\beta = 0.090, 0.12, 0.14$ , and  $0.18$ . Notice that, with the exception of the  $\beta = 0.090$  model, the density maxima are toroidal; similar structures were used as initial data in the collapse models of Rampp, Ruffert, & Müller (1998).

These initial models were introduced into 2 different 3-D hydrocodes. The first of these is the L code discussed in New, Centrella, & Tohline (2000), with a cylindrical  $(\varpi, z, \phi)$  grid of  $64 \times 64 \times 128$  zones. The second is the PPM code discussed by Brown (2000), with a Cartesian  $(x, y, z)$  grid of  $128 \times 128 \times 128$  zones. Both codes have the same resolution along the  $x$  and  $z$ -axes, with the equatorial radius  $R_E$  of the initial model extending out to zone 48 in  $x$ -direction. The cylindrical code imposes equatorial plane symmetry, whereas the Cartesian code imposes no symmetries. Random perturbations of 1% were imposed on the densi-

ties, and the models were evolved forward in time.

## 3. Results

The model with initial  $\beta = 0.14$  exhibits a dynamical instability that is very similar in simulations performed with both the cylindrical and Cartesian hydrocodes. These runs were stopped when the loss of mass from the edge of the grid became significant. Figure 2 shows density contours in the equatorial plane from the run with the cylindrical code. The green (lightest greyscale) contour in the first frame delineates the toroidal density maximum seen in Fig. 1. As time proceeds, this torus “pinches off” to leave a single high density region, indicative of an  $m = 1$  mode. At late times, the appearance of higher density contours signals that the dense region is starting to collapse. Time is measured in units of  $t_D = (R_E^3/GM)^{1/2}$ , which is the dynamical time for a *sphere* of mass  $M$  and radius  $R_E$ . For  $R_E \sim 200\text{ km}$ ,  $t_D \sim 6\text{ ms}$ . 3-D animations of the evolution of this model, using the same contour levels as in Figure 2 and looking down the  $z$ -axis towards the equatorial plane, are available for both the cylindrical and Cartesian runs. Additional animations, in which the model is viewed from the side, are also available for the cylindrical and Cartesian runs. [Note to editors: Here, the words “cylindrical” and “Cartesian” should link to the animations in each case.]

We can quantify the instability by examining various Fourier components in the density distribution. We examine the density in a ring of fixed  $\varpi$  and  $z$  using a complex azimuthal Fourier decomposition, where the amplitudes  $C_m$  of the various components  $m$  are defined by  $C_m(\varpi, z) = (1/2\pi) \int_0^{2\pi} \rho(\varpi, z, \varphi) e^{-im\varphi} d\varphi$  (Tohline, Durisen, & McCollough 1985). The normalized amplitude is then  $A_m = C_m/C_0$ , where  $C_0(\varpi, z) = \bar{\rho}(\varpi, z)$  is the mean density in the ring, and the phase angle of the  $m^{\text{th}}$  component is  $\phi_m(\varpi, z) = \tan^{-1} [\text{Im}(A_m)/\text{Re}(A_m)]$ . We write the phase angle  $\phi_m = \sigma_m t$ , where  $\sigma_m = d\phi/dt$  is the eigenfrequency and  $W_m = \sigma_m/m$  is the pattern speed of the  $m^{\text{th}}$  mode.

Figures 3 and 4 show the growth of the amplitudes  $|A_m|$  for the first four Fourier components in the runs with  $T/|W| = 0.14$  on the cylindrical and Cartesian hydrocodes, respectively. For the cylindrical code, these amplitudes were calculated in

the equatorial plane in a ring of width  $\Delta\varpi = 1/48$  at radius  $\varpi = 0.32$ ; see New, Centrella, & Tohline (2000) for details. For the Cartesian code, the amplitudes were computed on a circle of radius  $\varpi = 0.32$  using a nonuniform discretization, which avoids grid boundaries, and a linear interpolation of density.

Similar results were found in rings at other values of  $\varpi$ . The evolution in both runs is dominated by an exponentially growing  $m = 1$  mode (thick solid line). Once this mode is well into its exponential growth phase, an  $m = 2$  mode also develops, followed at later times by  $m = 3$  and  $m = 4$  modes. (The constant amplitude  $m = 4$  signal in the Cartesian run is due to the geometry of the numerical grid.) Since these modes grow rapidly on dynamical timescales, they signal dynamical instability. Numerical values for the growth rates, eigenfrequencies, and pattern speeds are shown in Table 1 for  $m = 1$  and  $m = 2$ . Notice that the cylindrical and Cartesian runs yield similar results and that the pattern speeds  $W_1 \sim W_2$ , indicating that the  $m = 2$  mode is a harmonic of the  $m = 1$  mode. Longer runs with larger grids and higher resolution are needed to obtain reliable values for the  $m = 3$  and  $m = 4$  modes.

The model with  $\beta = 0.18$  also exhibits dynamical instability. For the evolutions run with both codes, the  $m = 1$  mode grew at very close to the same rate, starting at about the same time; see Table 1. In the run on the cylindrical code, the modes  $m = 1, 2, 3$ , and  $4$  appear sequentially in time and  $W_1 \sim W_2$ , as in the model with  $\beta = 0.14$ . In the run on the Cartesian code, the  $m = 1$  and  $m = 2$  modes both grew at about the same rate, starting at about the same time; however,  $W_1 \neq W_2$ . At this stage, we do not understand this difference in the behavior of the  $m = 2$  mode in this case. We plan to investigate it using higher resolution simulations. The  $\beta = 0.12$  model was run for  $\sim 40t_D$ , at which time the  $m = 1$  mode was just beginning to grow; longer runs with higher resolution are needed to confirm the development of instability in this case. The model with  $\beta = 0.09$  was run for  $\sim 35t_D^{-1}$ , and showed no growing modes. In the event that we can confirm instability for  $\beta = 0.12$ , we will return to the  $\beta = 0.09$  case and run it further.

Previous studies of the  $m = 2$  bar-mode instability using the cylindrical hydrocode showed that

significant motion of the system center of mass could develop at late times, resulting in a spurious  $m = 1$  signal (New, Centrella, & Tohline 2000). For the simulations reported here, we monitored the position of the overall center of mass and verified that it underwent no systematic motion during the development of the  $m = 1$  mode, in both the cylindrical and Cartesian codes. When the runs with  $T/|W| = 0.14$  and  $T/|W| = 0.18$  were stopped, some small, spurious center of mass motion ( $< one zone$ ) had developed in both codes. This effect is possibly related to the loss of mass from the grid as the outer regions expand; runs with larger grids are needed to determine the late time behavior of these models. Previous studies of the bar instability using the Cartesian code (Brown 2000) showed that angular momentum losses due to numerical inaccuracies can be significant. For the  $\beta = 0.14$  and  $\beta = 0.18$  simulations with the Cartesian code, the artificial angular momentum losses amounted to less than 0.4% and 1.5%, respectively.

#### 4. Discussion

Our results demonstrate that dynamical instability can occur in differentially rotating polytropes with low values of  $\beta \gtrsim 0.14$ , and that this instability has a strong,  $m = 1$  character. Figure 1 shows that the unstable axisymmetric equilibria each have a torus of dense material centered on the rotation axis within the model. This suggests that this instability may be related to the ones found by Woodward, Tohline, & Hachisu (1994) and Tohline & Hachisu (1990) in their studies of polytropic tori with  $N = 3/2$ . We note that Pickett, Durisen, & Davis (1996) also found a dominant  $m = 1$  instability that set in at a relatively low  $\beta \gtrsim 0.20$ , in a centrally condensed model (without an off-center density maximum). Their model was an  $N = 3/2$  polytrope with an  $n' = 2$  rotation law. The  $n' = 2$  rotation law produces configurations with a strong concentration of angular momentum in the outer regions of the model. We plan to carry out more detailed studies to investigate the character of the unstable modes seen in our simulations and their properties for various values of  $N$  and the  $j$ -constant rotation law parameter  $d$ .

If such instability occurs in a centrifugally-hung

core, collapse to neutron star densities may result. Our simulations do show that the density is increasing at the end of the unstable runs. Further studies are needed to see how dense the remnant actually becomes, and whether the  $m = 1$  mode will result in the dense region moving at a velocity comparable to those of actual neutron stars (Popov, S. et al. 2000).

Dynamical instability will also produce gravitational radiation. Although longer runs are needed to obtain the full gravitational waveforms, we can estimate the properties of the gravitational wave emission from the initial stages of the instability. For a massive stellar core with  $M \sim 1.4M_{\odot}$  and  $R_E \sim 200\text{km}$ , the peak amplitude will occur at a frequency of roughly  $f \sim 200\text{Hz}$ . This peak amplitude will be  $h \sim 10^{-24}r_{20}^{-1}$  for  $\beta = 0.14$ , and  $h \sim 10^{-23}r_{20}^{-1}$  for  $\beta = 0.18$ . Here,  $r_{20}$  is the distance to the source in units of 20 Mpc. Emission from such unstable cores may be detectable with advanced ground-based interferometers, such as LIGO-II. An even more optimistic scenario for detectable gravitational radiation occurs if these instabilities arise in supermassive stars<sup>5</sup> (New & Shapiro 2000). For example, if the instability occurs when a supermassive star contracts to the point that  $(GM/Rc^2) \sim 1/15$ , an approximate value for uniformly rotating stars (Baumgarte & Shapiro 1999), we estimate the frequency of the gravitational radiation to be  $f \sim 3.5 \times 10^{-3}\text{Hz}$ , with amplitude  $h \sim 10^{-18}r_{20}^{-1}$  for  $\beta = 0.14$  and  $h \sim 10^{-17}r_{20}^{-1}$  for  $\beta = 0.18$ . Such signals would be easily detectable by the space-based LISA detector.

We thank K. Thorne and J. Tohline for stimulating discussions, and E. Mamikonyan for assistance with the animations. This work was supported in part by NSF grants PHY-9722109, PHY-0070892, NSF cooperative agreement ACI-9619020 through computing resources provided by the National Partnership for Advanced Computational Infrastructure (NPACI) at the San Diego Supercomputer Center (SDSC), and the North Carolina Supercomputing Center (NCSC). A portion of this work was performed under the auspices of the U.S. Department of Energy by Los

Alamos National Laboratory under contract W-7405-ENG-36. The cylindrical simulations were run on the T3E at SDSC, and the Cartesian models on the T90 at NCSC.

## REFERENCES

- Baumgarte, T. & Shapiro, S. 1999, ApJ, 526, 941
- Brown, J. D. 2000, Phys. Rev. D, in press (gr-qc/0004002)
- Eriguchi, Y. & Müller, E. 1985, A&A, 147, 161
- Hachisu, I. 1986, ApJS, 61, 479
- Hayashi, A., Eriguchi, Y., and Hashimoto, M. 1998, ApJ, 492, 286
- Hayashi, A., Eriguchi, Y., and Hashimoto, M. 1999, ApJ, 521, 376
- Imamura, J., Toman, J., Durisen, R., Pickett, B., & Yang, S. 1995, ApJ, 444, 363
- Müller, E. and Eriguchi, Y. 1985, A&A, 152, 325
- New, K., Centrella, J., and Tohline, J. 2000, Phys. Rev. D, in press (astro-ph/9911525)
- New, K. & Shapiro, S. 2000, ApJ, submitted (see also astro-ph/0009095)
- Pickett, B., Durisen, R., and Davis, G. 1996, ApJ, 458, 714
- Popov, S., Colpi, M., Treves, A., Turolla, R., Lipunov, V., & Prokhorov, M. 2000, ApJ, accepted (astro-ph/9910114)
- Rampp, M., Müller, E., & Ruffert, M. 1998, A&A, 332, 969
- Rasio, F. & Shapiro, S. 1992, ApJ, 401, 226
- Schutz, B. 1989, Class. Quantum Gravity, 6, 1761
- Shibata, M., Baumgarte, T., & Shapiro, S. 2000, ApJ, in press (astro-ph/0005378)
- Stergioulas, N. & Friedman, J. 1998, ApJ, 492, 301
- Tassoul, J. 1978, Theory of Rotating Stars (Princeton: Princeton University Press)

<sup>5</sup>We note that the appropriate equation of state for supermassive stars is the  $n = 3$  polytropic equation of state.

Thorne, K. 1996, in Proceedings of IAU Symposium 165, Compact Stars in Binaries, ed. J. van Paradjis, E. van den Heuvel, & E. Kuulkers (Dordrecht: Kluwer)

Tohline, J. 1984, ApJ285, 721

Tohline, J., Durisen, R., & McCollough, M. 1985, ApJ, 298 220

Tohline, J. & Hachisu, I. 1990, ApJ, 361, 394

R. Wagoner, 1984 ApJ278, 345

Woodward, J., Tohline, J., & Hachisu, I. 1994, ApJ, 420, 247

X. Zhuge, J. Centrella, & S. McMillan 1994, Phys. Rev. D, 50, 6247

Zwergler, T. & Müller, E. 1997, A&A, 320, 209

Fig. 1.— Density contours are shown in the  $x - z$  plane for 4 models with  $d = 0.2$  and  $N = 3.33$ . The initial maximum density is normalized to unity, and the contours are at levels of 0.9, 0.1, 0.01, and 0.001

Fig. 2.— 2-D density contours in the equatorial plane are shown for the model with  $\beta = 0.14$  run on the cylindrical code. The contour levels are 0.01 (purple), 0.1 (blue), 0.9 (green), 2 (yellow), and 4 (off-white) times the maximum density at the initial time, which is normalized to unity. In the greyscale version of this figure, the density decreases as the darkness of the shading increases.

Fig. 3.— The growth of the amplitudes  $|A_m|$  for  $m = 1$  (thick solid line),  $m = 2$  (thin solid line),  $m = 3$  (dashed line), and  $m = 4$  (dotted line) is shown for the model with initial  $T/|W| = 0.14$  run on the cylindrical hydrocode. These amplitudes were calculated in the equatorial plane for a ring with radius  $\varpi = 0.32$ .

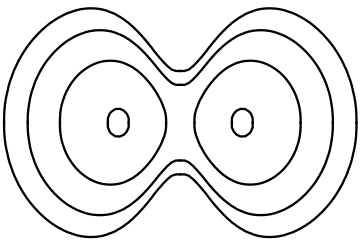
Fig. 4.— Same as Figure 3, except that the model was evolved on the Cartesian hydrocode.

code	$\beta$	$d \ln  A_1 /dt$ [ $t_D^{-1}$ ]	$d \ln  A_2 /dt$ [ $t_D^{-1}$ ]	$\sigma_1$ [ $t_D^{-1}$ ]	$\sigma_2$ [ $t_D^{-1}$ ]	$W_1$ [ $t_D^{-1}$ ]	$W_2$ [ $t_D^{-1}$ ]
cyl	0.14	0.40	0.92	3.6	7.2	3.6	3.6
cart	0.14	0.35	0.90	3.5	7.2	3.5	3.6
cyl	0.18	0.99	1.8	3.3	6.6	3.3	3.3
cart	0.18	0.98	1.1	3.2	2.4	3.2	1.2

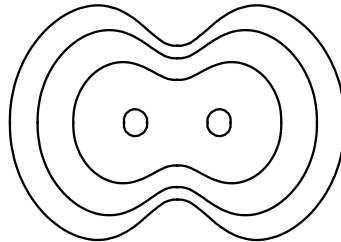
Table 1: The growth rates, eigenfrequencies, and pattern speeds for the  $m = 1$  and  $m = 2$  modes are given in a ring at radius  $\varpi = 0.32$  in the equatorial plane.

This 2-column preprint was prepared with the AAS L<sup>A</sup>T<sub>E</sub>X macros v5.0.

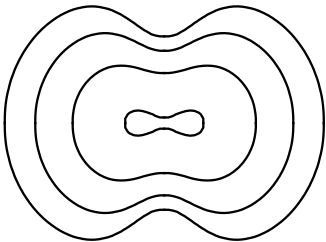
$$T / |W| = .18$$



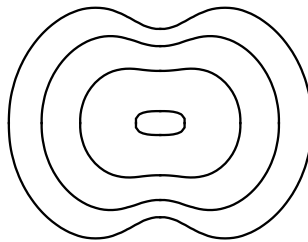
$$T / |W| = .14$$



$$T / |W| = .12$$



$$T / |W| = .09$$



This figure "fig2.jpg" is available in "jpg" format from:

<http://arxiv.org/ps/astro-ph/0010574v1>

